Chinese Chemical Letters 31 (2020) 1183–1187

Contents lists available at ScienceDirect

Chinese Chemical Letters

journal homepage: www.elsevier.com/locate/cclet

Communication

An iridium(III)-palladium(II) metal-organic cage for efficient mitochondria-targeted photodynamic therapy

Chaojie Li[a,1], Yaping Wang[a,1], Yulin Lu[a], Jing Guo[a], Chengyi Zhu[a], Haozhe He[b], Xiaohui Duan[c], Mei Pan[a,*], Chengyong Su[a]

[a] MOE Laboratory of Bioinorganic and Synthetic Chemistry, Lehn Institute of Functional Materials, School of Chemistry, Sun Yat-Sen University, Guangzhou 510275, China
[b] School of Materials Science and Engineering and School of Chemistry, Sun Yat-Sen University, Guangzhou 510275, China
[c] Sun Yat-Sen Memorial Hospital, Sun Yat-Sen University, Guangzhou 510120, China

ARTICLE INFO

Article history:
Received 2 August 2019
Received in revised form 11 September 2019
Accepted 18 September 2019
Available online 18 September 2019

Keywords:
Metal-organic cage
Photodynamic therapy
Mitochondria-targeted
Ir(III) metalloligand
Two-photon

ABSTRACT

An Ir_8Pd_4-heteronuclear metal-organic cage (MOC-51) was assembled from bipodal metalloligand $[Ir(ppy)_2(qpy)(BF_4)]$ (qpy = 4,4′:2′,2″:4″,4‴-quaterpyridine; ppy = 2-phenylpridine) with Pd(II) salt. The cubic barrel shaped MOC shows one-photon and two-photon excited deep-red emission, as well as large singlet oxygen quantum yields under visible light irradiation, therefore exhibiting great potentials in organelles-targeted cell imaging and photodynamic therapy (PDT). Compared with the Ir(III) metalloligand, the Ir_8Pd_4-MOC showed less dark toxicity and higher mitochondria-targeting efficiency. The localization in mitochondria overcomes the limitation of short lifetime and diffusion distance of ROS in cell, thus improved PDT effect can be obtained in low light dose usage of the MOC. This study presents the first case of Ir-based metal-organic cages for bio-applications in successful integration of imaging diagnosis and photodynamic therapy

Metal-organic cages (MOCs) have well-defined shapes and cavities, and possess potential applications in confined space catalysis [1], separation [2], photocatalytic hydrogen production [3], fluorescence [4], and so on [5,6]. Among which, MOCs assembled from metalloligand strategy can be afforded with structural controllability and predictability, due to the composition and configuration of metalloligands are generally stable during secondary assembly. Meanwhile, ensembles of the obtained MOCs will bring unique chemical, physical and biological properties superior than the precursors, owing to the synergistic effects among different components and "concentration effect" of the uniquely confined cage configuration [7–10]. However, up to now, the above advantages have been barely studied in the bio-applications of MOCs [11].

Iridium(III) complexes have excellent photoelectric and remarkable chemo-physical properties, such as great chemical stability, high quantum yield and good cell permeability, so they have attracted extensive attention in the field of biological imaging and sensing probes [12]. In addition, in recent years, Ir(III) complexes were also reported to be good photosensitizers for the photodynamic therapy (PDT) [13–16]. It is expected that metal-organic cages assembled from Ir(III) metalloligands can not only possess controllable shapes and inner cavities, but also hold and optimize the pristine property of Ir(III) complexes. As far as we know, the successful assembly of Ir(III)-based MOCs remains quite rare, even less for their bio- applications in cell imaging and cancer therapy [17–20]. To achieve this purpose, apart from good photophysical properties, the following concerns should also be considered for the MOCs, including chemical stability, water-/lipo-solubility, bio-compatibility, long- term toxicity, and so on. Bearing the above considerations in mind, we report herein the stepwise assembly of an Ir(III)–Pd(II) MOC from a predesigned bipodal Ir(III) metalloligand. Inspired by its good one-photon and two-photon luminescence, as well as large singlet oxygen quantum yield, the MOC was applied in mitochondria-targeted cell imaging and photodynamic therapy successfully, presenting the first example of Ir(III)-based MOC in PDT field.

The bipodal metalloligand $[Ir(ppy)_2(qpy)](BF_4)$ solvents (Irqpy), possessing two coordinated 2-phenylpyridine moieties, one coordinated bipyridine linker, and two uncoordinated pyridine (Py) pendants, was prepared by reaction of qpy (4,4′:2′,2″:4″,4‴-

* Corresponding author.
E-mail address: panm@mail.sysu.edu.cn (M. Pan).
[1] These authors contributed equally to this work.

https://doi.org/10.1016/j.cclet.2019.09.034
1001-8417/

quaterpyridine, Scheme S1 in Supporting information) with $[Ir(ppy)_2(\mu\text{-}Cl)]_2$, and the structure was unambiguously confirmed by single-crystal diffraction analyses, (Fig. S1 and Tables S1–S3 in Supporting information). Irqpy was further assembled with $Pd(CH_3CN)_4(BF_4)_2$ at 80 °C to result in formation of an Ir(III)-Pd(II) heteronuclear cage $[Pd_4(Irqpy)_8]$ $(BF_4)_{16}$ solvents, MOC-51, in which Ir(III) centers are 6-coordinated, and Pd(II) ions are 4-coordinated (Fig. 1a and Fig. S1). The composition of the cage structure can be further proved by detailed solution NMR and MS study (Figs. S2–S6 in Supporting information).

First, the solution assembly process for MOC-51 was monitored by ^1H NMR titration in DMSO-d_6 (Fig. 1b). It can be seen that the proton signals of pure Irqpy metalloligand can be divided into eleven sets. When $Pd(CH_3CN)_4(BF_4)_2$ is added to a solution of Irqpy, new proton signals appeared besides those of "free" Irqpy ligand. Along with the titration process, broadness of the NMR signals is observed, clearly indicating the complexation between Irqpy and Pd(II) ions, and formation of dynamics for large molecules with slow rotational diffusion. When the concentration of Pd(II) was low (Pd:Irqpy ratio below 3:8), the ^1H NMR spectra exhibit signals for the mixture of Pd-coordinated and free Irqpy metalloligand. When the ratio increases above 4:8, the proton peaks no longer change, which indicates that a thermodynamically $[Pd_4(Irqpy)_8]^{16+}$ cage is preferentially formed. Compared with the free Irqpy metalloligand, the proton peaks of the $[Pd_4(Irqpy)_8]^{16+}$ cage show different shifts (Fig. S2), which are coincident with the NMR titration results. From the $^1H-^1H$ COSY spectra, proton correlation can be established for the pendant pyridine peaks (Fig. S3). As we can see, upon formation of the cage, the signals of pendant pyridine H-atmos (b, c) are moved downfield, due to the coordination-induced effect between Py-donor and Pd(II). While other proton signals (a, i, m) manifest upfield shift, showing increase of shielding effect after MOC formation.

^1H DOSY NMR spectroscopy (Fig. S4) clearly indicates that a single substance is formed in the DMSO-d_6 solution of MOC- 51, which has a diffusion coefficient of 7.1×10^{-11} m^2/s. From the value of diffusion coefficient, it can be seen that the structure is much larger than that of the Irqpy metalloligand (1.7×10^{-10} m^2/s). The calculated hydrodynamic radius (r_s) of the MOC-51 is 15 Å. In order to further prove the structure of $[Pd_4(Irqpy)_8]^{16+}$ cage in solution, high-resolution electrospray ionization time-of-flight mass spectrometry (HR-ESI-TOF- MS) was measured. Figs. S5 and S6 show a series of isotopically resolved peaks related with different $[Pd_4(Irqpy)_8]^{16+}$ plus anions species, which can be matched well with the simulated spectra. For example, the peak at 1099.006 can be attributed to heptavalent $[(C_{42}H_{30}IrN_6)_8Pd_4(BF_4)_9]^{7+}$, which can be confirmed by comparing experimental data with simulated data. Based on the above results, molecular structure of MOC-51 was simulated as shown in Fig. 1a. As we can see, eight Irqpy metalloligands form a cubic barrel, and each Irqpy extends two pendant pyridines to link with Pd(II) ions. In general, an Ir_8Pd_4 cage is formed, which possesses suitable molecular size (~1.5 nm) and high valence states (+16). This may contribute to the cell uptaking and photodynamic therapy applications, as will be further explored below.

The UV–vis absorption spectra of the metalloligand and MOC-51 were measured in DMSO solution as shown in Fig. 2a. As we can see, the two spectra are basically the same, with only slight difference in molar extinction coefficient. In the UV region, $Pd_4(Irqpy)_8$ cage exhibits intense absorption bands between 250 nm and 350 nm, originated from the π-π^* transitions of ppy and qpy. Lower absorption from 350 nm to 450 nm can be attributed to intramolecular charge transfer (ILCT). Characteristically for Ir(III) compounds, broad and lower intensity bands are observed for the cage from 450 nm to 550 nm, which can be attributed to MLCT (metal-to-ligand charge transfer) transitions from Ir^{III} metal centers to ppy and qpy organic ligands.

The photoluminescent peak shape and position of MOC-51 are basically the same as Irqpy metalloligand both in DMSO and solid state at room temperature, which indicates that the emission of cage comes from the transition of ^{3}MLCT of Irqpy. In the solid state, Irqpy and MOC-51 exhibit wide band emissions centered at 665 nm (Fig. S7 in Supporting information), which fall into the deep-red region. Importantly, the excitation can be in the visible blue light region of 470 and 430 nm for MOC-51 and Irqpy in DMSO solution, respectively, showing great advantage to be applied in bioimaging. The decay lifetimes were found to be 57 and 19 ns at room temperature (Table S4 and Fig. S8 in Supporting information). The decay lifetime of MOC-51 increased to 537 ns at 77 K low temperature (Fig. S9 in Supporting information), which sufficiently shows the characteristics of the ^{3}MLCT and lowest excitation triplet state phosphorescence of Ir(III) complexes. Compared with the solid state, the emissions of Irqpy and MOC-51 have a similar peak shape and position in the DMSO solution, with maxima at 654/658 nm (Fig. 2b, Table S4), slightly blue-shifted compared with the solid state. Longer decay lifetimes of 158 and 141 ns (Fig. S10 in Supporting information) are observed for Irqpy and MOC-51 in DMSO solution at room temperature, respectively. Compared with Irqpy metalloligand, the quantum yield (Φ_{em}) of MOC-51 is reduced to 3.5% due to the quenching effect of Pd-coordination, but still suitable for the bioimaging study as shown below.

Irqpy and MOC-51 also show two-photon excited emission spectra (Fig. S11 in Supporting information), with the pisitions and shapes similar to that of the one-photon emission. The slopes of

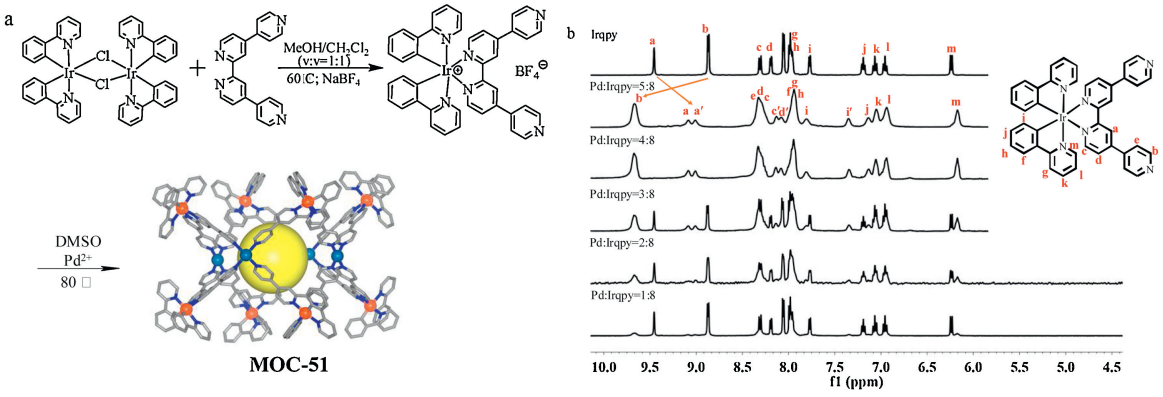

Fig. 1. (a) Synthetic route of Ir_8Pd_4-cage (MOC-51) from Irqpy metalloligand (for the simulated MOC structure, Ir, orange, Pd, turquoise, C, gray, N, blue, and the yellow ball represents inside cavity, hydrogen atoms, anions and solvents are omitted for clarity). (b) ^1H NMR titration of Irqpy metalloligand (top) with the addition of $Pd(CH_3CN)_4(BF_4)_2$ in DMSO-d_6 at 298 K.

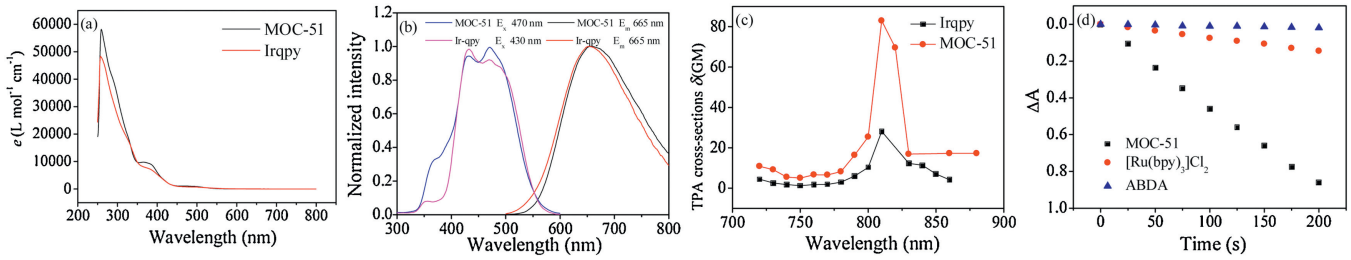

Fig. 2. (a–c) Photophysical spectra of Irqpy metalloligand (1×10^{-5} mol/L) and MOC-51 (1.25×10^{-6} mol/L) in DMSO solution at room temperature. (a) UV–vis absorption spectra; (b) Photoluminescent excitation and emission spectra; (c) TPA cross-section at different excitation wavelengths from 720 nm to 880 nm. (d) Comparison of the quantum yields for $^1O_2$ production (Φ_Δ) of MOC-51 and $[Ru(bpy)_3]Cl_2$ stantard in water solution.

the logarithm of the two-photon induced fluorescence intensity and the excitation power are approximately 2, indicating that the emissions are indeed *via* two-photon process (Fig. S12 in Supporting information). The two-photon absorption (TPA) cross section were further measured from 720 nm to 860 nm in DMSO by using rhodamine B (4×10^{-4} mol/L) as the reference. The maximum TPA cross-sections (δ_{max}, λ_{ex} = 820 nm) were measured to be 28 and 83 GM for Irqpy and MOC-51, respectively (Fig. 2c), showing great potentials for two-photon imaging in living cells.

To research the singlet oxygen generation efficiency of MOC-51, the quantum yields for $^1O_2$ production under a 425 nm xenon lamp with filter was measured in water using a steady-state method with 9,10- anthracenediyl-bis-(methylene) dimalonic acid (ABDA) as the $^1O_2$ indicator and $[Ru(bpy)_3]Cl_2$ as the standard substance (Φ_Δ = 0.18 in H_2O, Fig. 2d, Figs. S13 and S14 in Supporting information). The Φ_Δ values of MOC-51 was calculated to be 0.46. This rather high value compared with reported iridium complexes under similar near-neutral pH conditions indicates that MOC-51 is promising as an efficient photodynamic therapy photosensitizer [13–16].

Due to the excellent photophysical properties of MOC-51, the cellular imaging in Hela cells was conducted by using laser scanning confocal microscopy. As shown in Fig. S15 (Supporting information), strong red luminescence was observed in the cytoplasm both under the one-photon and two-photon excitations after incubated with MOC-51 for 2 h, suggesting the good physiological stability and high cellular uptake efficiency of the cage compound. Then the subcellular localization of MOC-51 with commercial mitochondrial dye Mito-Tracker Green (MTG), lysosome dye Lyso-Tracker Red (LTR) or the nucleus dye DAPI was further performed. As shown in Fig. 3a, a great superimposition pattern was observed for MTG and MOC-51 treated cells with a

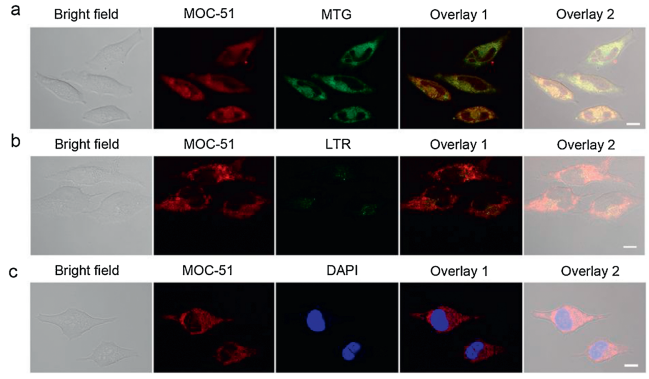

Fig. 3. Cellular colocalization images of Hela cells incubated with (a) MOC-51 (6 μmol/L, 3 h) and MTG (150 nmol/L, 30 min), (b) LTR (150 nmol/L, 30 min) or (c) DAPI (8 μg/mL, 20 min). MOC-51: λ_{ex} = 405 nm, λ_{em} = 670 ± 20 nm; MTG: λ_{ex} = 488 nm, λ_{em} = 516 ± 20 nm; LTR: λ_{ex} = 548 nm, λ_{em} = 590 ± 20 nm; DAPI: λ_{ex} = 405 nm, λ_{em} = 460 ± 20 nm. The scale bar is 20 μm.

relative high correlation coefficient of 0.88, indicating that MOC-51 was localized in the mitochondrial of living Hela cells. In comparison, poor overlap was found between MOC-51 and LTG or DAPI treated cells (Figs. 3b and c), which further demonstrated the specific mitochondrial targeting of MOC-51. In addition, the cellular colocalization of Irqpy was also carried out (Fig. S16 in Supporting information). The results showed that Irqpy were also specifically localized in the mitochondrial, but with smaller correlation coefficient (0.76) than MOC-51, which may be attributed to the higher positive charge (+16) of MOC-51 due to the introduction of Pd(II) ions.

As MOC-51 was targeted in mitochondrial, the mitochondrial membrane potentials (MMP) of Hela cells incubated with MOC-51 were determined before and after the light irradiation (425 nm, 7.2 J/cm^2). The JC-1 assay was performed to evaluate the MMP changes [21]. JC-1 will accumulate in mitochondria at high MMP and form aggregation state which exhibits red fluorescence. However, at low MMP, JC-1 fails to aggregate in the mitochondrial, and forms monomer state which emits green fluorescence. As shown in Fig. 4a, compared to the control group, MOC-51 treated Hela cells exhibited obvious green fluorescence after light irradiation, indicating the decrease of MMP, which was associated with the early sign of cell apoptosis [22]. The obvious fluorescence changes of JC-1 further confirmed that the reactive oxygen species (ROS) generated in photodynamic therapy could decrease the MMP, thus resulting in the apoptosis and death of Hela cells. Since ROS possessed short lifetime and restricted range of diffusion [23], the PDT effect could be improved by the selective accumulation of MOC-51 in mitochondrial.

In order to verify whether MOC-51 had a highly efficient photodynamic effect on cells, the cytotoxicity of Hela cells under dark and light irradiation conditions were both measured by MTT assay. As shown in Fig. 4b, MOC-51 showed no obvious cytotoxicity in the dark for 48 h ($IC_{50} \geq$ 015 μmol/L), which is an important precondition for the well-suitable photodynamic therapy agent. However, high phototoxicity to Hela cells was observed ($IC_{50} \geq$ 1.82 μmol/L) when exposed to an extremely small light dose of 7.2 J/cm^2 at 425 nm. Comparatively, using the same Ir(III) amount-containing MOC-51 and Irqpy samples, the Irqpy treated Hela cells showed apparent dark cytotoxicity although Irqpy also possessed a similar PDT performance as the MOC-51 (Fig. 4c). As the dark cytotoxicity between MOC-51 and Irqpy was found to be obviously different, inductively coupled plasma mass spectrometry (ICP-MS) method was employed to precisely estimate cellular uptake level between MOC-51 and Irqpy. As shown in Fig. S17 (Supporting information), both MOC-51 and Irqpy exhibited time-dependent cellular uptake, and the maximum uptake efficiency reached to 9.45% and 3.84% at 24 h, respectively. The difference on the uptake efficiency between MOC-51 and Irqpy implied that MOC-51 was more favorable for uptaking by mitochondrial than the Irqpy metalloligand, which may be resulted from the appropriate molecular size and increased valence states after MOC formation.

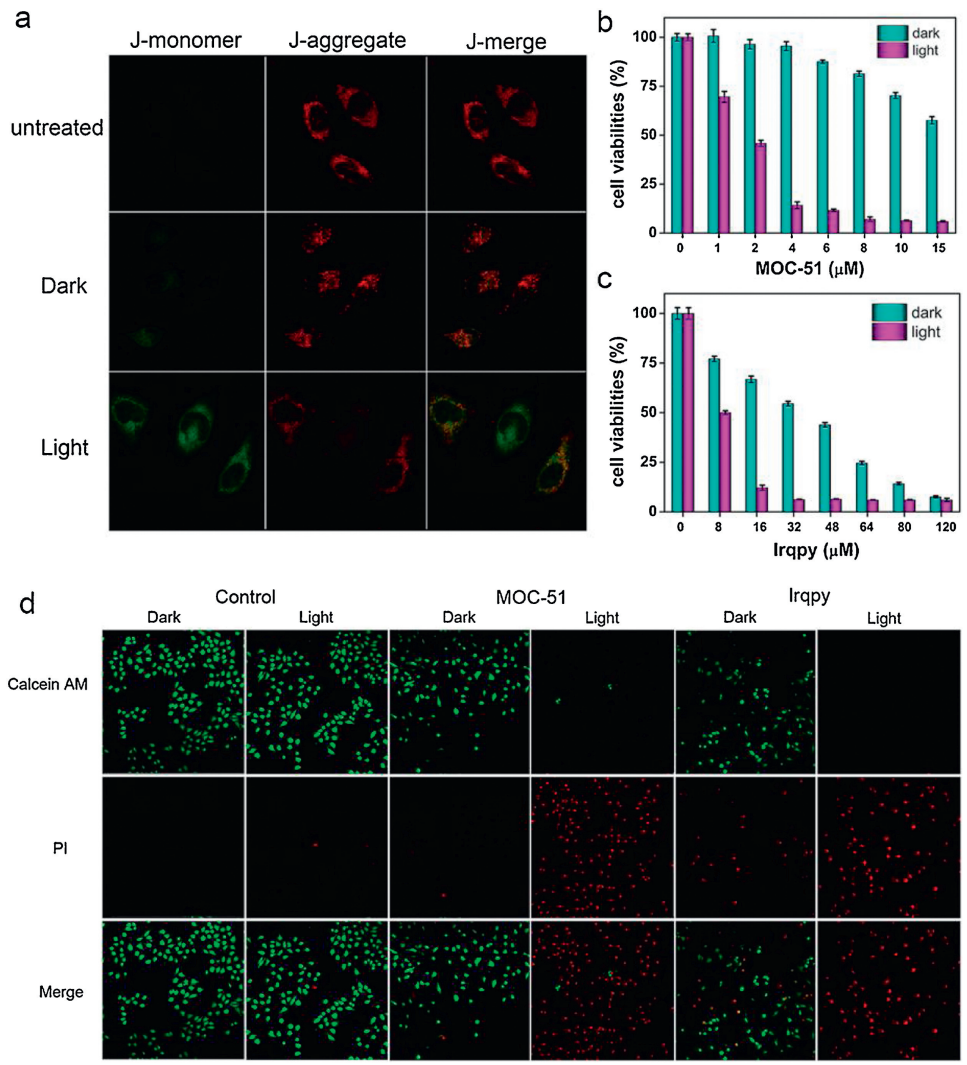

Fig. 4. (a) Confocol images of Hela cells after JC-1 staining treated with MOC-51 with or without light irradiation. Scale bar: 20 μm. The dark cell viabilities and phototoxicity of Hela cells treated with MOC-51 (b) and Irqpy (c), respectively. (d) Confocal images of MOC-51 (10 μmol/L) and Irqpy (80 μmol/L) in Hela cells before and after irradiation. The cells were double-stained by calcein AM and PI.

In addition, cells only treated with 1% DMSO as the blank control group exhibited negligible difference on the cytotoxicity with or without the light irradiation condition (Fig. S18 in Supporting information). And cisplatin as the positive control showed little phototoxicity, either (Fig. S19 in Supporting information). It is noted that under the same light irradiation (425 nm, 7.2 J/cm^2), the $Ru(bqy)_3Cl_2$ also showed negligible phototoxicity upon such small light dose (Fig. S20 in Supporting information). Compared with $Ru(bqy)_3Cl_2$, the singlet oxygen quantum yield of MOC-51 is higher, which indicates that MOC-51 has better photodynamic effect, as revealed before in Figs. S13 and S14.

To further confirm the *in vitro* PDT effect of MOC-51, the Hela cells was stained with calcein-AM and PI to directly visualize the cell viability. The green fluorescence from calcein-AM and red fluorescence from PI indicated the live and dead cells, respectively. As shown in Fig. 4d, the cells incubated with Irqpy showed some dark cytotoxicity while the MOC-51 showed little cell death as compared to the untreated cells group, while significant cell death was both observed against the cells with the incubation of MOC-51 and Irqpy irradiated by light. These observations are consistent with the result of cell viabilities by MTT method, and further revealed that MOC-51 could serve as an excellent PDT agent due to the excellent properties such as low dark toxicity and high phototoxicity.

Then the intracellular singlet oxygen was also evaluated by using the 2,7-dichlorofluorescein diacetate (DCFH-DA) as the ROS indicator. The non-fluorescent DCFH could be oxidized by the intracellular ROS to form the green-emitting DCF, thus the cellular ROS level could be reflected based on the fluorescence intensity of DCF. As shown in Fig. S21 (Supporting information), cell treated with light and MOC-51 in the dark showed weak fluorescence, while the cells incubated with MOC-51 upon 425 nm light irradiation exhibited much strong green fluorescence than that of those control cells, further indicating the ROS played a crucial role in the PDT of MOC- 51.

In summary, a cubic barrel shaped Ir-Pd heteronuclear metal-organic cage (MOC-51) was assembled from iridium(III) metalloligand, which shows one-photon and two-photon excited deep-red emission, and large singlet oxygen quantum yield under visible light irradiation. The Ir-based MOC was applied for bioimaging and photodynamic therapy for the first time. Effectively, MOC-51 reveals lower dark toxicity and higher mitochondria-targeted light toxicity compared with the precursor Ir-metalloligand, showing advantages of the synergistic effects of MOCs. These findings suggested the feasibility of MOCs on the integration of luminescence diagnosis and cancer therapy, which may lead to the evolution of MOCs and related materials in bio-applications, and so on.

Acknowledgments

This work was supported by the National Natrual Science Foundation of China (NSFC, Nos. 21771197, 21720102007, 21821003), Local Innovative and Research Teams Project of Guangdong Pearl River Talents Program (No. 2017BT01C161), and FRF for the central universities.

Appendix A. Supplementary data

Supplementary material related to this article can be found, in the online version, at doi:https://doi.org/10.1016/j.cclet.2019.09.034.

References

[1] (a) D.M. Kaphan, M.D. Levin, F.D. Toste, et al., Science 350 (2015) 1235;
(b) K. Yan, M. Fujita, Science 350 (2015) 1165–1166;
(c) J. Jiao, C. Tan, Z. Li, et al., J. Am. Chem. Soc. 140 (2018) 2251–2259;
(d) L.X. Cai, S.C. Li, D.N. Yan, et al., J. Am. Chem. Soc. 140 (2018) 4869–4876.
[2] (a) K. Wu, K. Li, Y.J. Hou, et al., Nat. Commun. 7 (2016) 10487;
(b) D. Luo, X.Z. Wang, C. Yang, X.P. Zhou, D. Li, J. Am. Chem. Soc. 140 (2018) 118–121.
[3] (a) S. Chen, K. Li, F. Zhao, et al., Nat. Commun. 7 (2016) 13169;
(b) X. Jing, C. He, Y. Yang, C. Duan, J. Am. Chem. Soc. 137 (2015) 3967–3974.
[4] (a) X. Yan, T.R. Cook, P. Wang, F. Huang, P.J. Stang, Nat. Chem. 7 (2015) 342;
(b) P.D. Frischmann, V. Kunz, F. Würthner, Angew. Chem. Int. Ed. 54 (2015) 7285–7289;
(c) B. Roy, A.K. Ghosh, S. Srivastava, P. D'Silva, P.S. Mukherjee, J. Am. Chem. Soc. 137 (2015) 11916–11919;
(d) X.F. Jiang, F.K.W. Hau, Q.F. Sun, S.Y. Yu, V.W.W. Yam, J. Am. Chem. Soc. 136 (2014) 10921–10929.
[5] (a) C.J. Brown, F.D. Toste, R.G. Bergman, K.N. Raymond, Chem. Rev. 115 (2015) 3012–3035;
(b) L.J. Chen, H.B. Yang, M. Shionoya, Chem. Soc. Rev. 46 (2017) 2555–2576;
(c) S.H.A.M. Leenders, R. Gramage- Doria, B. de Bruin, J.N.H. Reek, Chem. Soc. Rev. 44 (2015) 433–448;
(d) S. Zarra, D.M. Wood, D.A. Roberts, J.R. Nitschke, Chem. Soc. Rev. 44 (2015) 419–432;
(e) M. Pan, K. Wu, J.H. Zhang, C.Y. Su, Coord. Chem. Rev. 378 (2019) 333–349.
[6] (a) H. Li, Z.J. Yao, D. Liu, G.X. Jin, Coord. Chem. Rev. 293-294 (2015) 139–157;
(b) Y.Y. Zhang, W.X. Gao, L. Lin, G.X. Jin, Coord. Chem. Rev. 344 (2017) 323–344.
[7] K. Li, L.Y. Zhang, C. Yan, et al., J. Am. Chem. Soc. 136 (2014) 4456–4459.
[8] D. Rota Martir, D.B. Cordes, A.M.Z. Slawin, et al., Chem. Commun. 54 (2018) 6016–6019.
[9] D. Rota Martir, D. Escudero, D. Jacquemin, et al., Chem. -Eur. J. 23 (2017) 14358–14366.
[10] W. Cullen, A.J. Metherell, A.B. Wragg, et al., J. Am. Chem. Soc. 140 (2018) 2821–2828.
[11] (a) N. Ahmad, H.A. Younus, A.H. Chughtai, F. Verpoort, Chem. Soc. Rev. 44 (2015) 9–25;
(b) H. Vardhan, M. Yusubov, F. Verpoort, Coord. Chem. Rev. 306 (2016) 171–194;
(c) C.Y. Zhu, M. Pan, C.Y. Su, Isr. J. Chem. 59 (2019) 209–219.
[12] D. Rota Martir, E. Zysman-Colman, Coord. Chem. Rev. 364 (2018) 86–117.
[13] L. He, Y. Li, C.P. Tan, R.R. Ye, et al., Chem. Sci. 6 (2015) 5409–5418.
[14] D. Maggioni, M. Galli, L. D'Alfonso, et al., Inorg. Chem. 54 (2015) 544–553.
[15] J.S. Nam, M.G. Kang, J. Kang, et al., J. Am. Chem. Soc. 138 (2016) 10968–10977.
[16] X. Tian, Y. Zhu, M. Zhang, et al., Chem. Commun. 53 (2017) 3303–3306.
[17] O. Chepelin, J. Ujma, X. Wu, et al., J. Am. Chem. Soc. 134 (2012) 19334–19337.
[18] N. Singh, J.H. Jo, Y.H. Song, et al., Chem. Commun. 51 (2015) 4492–4495.
[19] X. Li, J. Wu, C. He, R. Zhang, C. Duan, Chem. Commun. 52 (2016) 5104–5107.
[20] S. Oldknow, D.R. Martir, V.E. Pritchard, et al., Chem. Sci. 9 (2018) 8150–8159.
[21] W. Lv, Z. Zhang, K.Y. Zhang, et al., Angew. Chem. Int. Ed. 55 (2016) 9947–9951.
[22] L. Rui, Y. Xue, Y. Wang, Y. Gao, W. Zhang, Chem. Commun. 53 (2017) 3126–3129.
[23] Z. Zhou, J. Liu, T.W. Rees, et al., PNAS 115 (2018) 5664.